Three-Dimensional Imaging of Individual Dopant Atoms in $SrTiO_3$

Jinwoo Hwang,[1,*] Jack Y. Zhang,[1] Adrian J. D'Alfonso,[2] Leslie J. Allen,[2] and Susanne Stemmer[1,†]

[1]*Materials Department, University of California, Santa Barbara, California 93106-5050, USA*

[2]*School of Physics, University of Melbourne, Victoria 3010, Australia*

(Received 1 November 2013; revised manuscript received 20 November 2013; published 26 December 2013)

We report on three-dimensional (3D) imaging of individual Gd dopant atoms in a thin (~2.3 nm) foil of $SrTiO_3$, using quantitative scanning transmission electron microscopy. Uncertainties in the depth positions of individual dopants are less than 1 unit cell. The overall dopant concentration measured from atom column intensities agrees quantitatively with electrical measurements. The method is applied to analyze the 3D arrangement of dopants within small clusters containing 4–5 Gd atoms.

DOI: 10.1103/PhysRevLett.111.266101 PACS numbers: 68.37.Ma

Obtaining three-dimensional (3D), atomic-scale information of dopant atom locations is of great importance for optimizing nanoscale devices. For example, individual dopant atoms already control the performance of current generations of silicon transistors and spintronic devices [1–3]. Spherical aberration (C_s) correction in transmission electron microscopy allows for subangstrom lateral resolution [4–7] and similar vertical resolution for materials consisting of two atomic layers [8]. Individual dopant atoms inside crystals can be detected by atomic-number (Z) sensitive high-angle annular dark-field (HAADF) imaging [9–16] and/or electron energy loss spectroscopy [17–20] in scanning transmission electron microscopy (STEM). Obtaining 3D information remains, however, challenging, because of the finite depth of focus that limits the depth resolution in through-focal series or confocal approaches [10,21–23], even with recent improvements (~5 nm for C_s-corrected probes) [24–26]. An alternative method is quantitative HAADF-STEM, which measures the signal from individual atom columns on an absolute scale for direct comparison with image simulations [27–29]. Information can be extracted from a single image, thereby avoiding alignment issues of approaches that require multiple images. In this Letter, we show that quantitative STEM allows for measuring the 3D arrangements of Gd atoms in a $SrTiO_3$ foil.

We first discuss the challenges in obtaining interpretable, depth-resolved information from HAADF-STEM image intensities. Thin TEM foils are required to maximize the dopant visibility [9,13], which also depends on the Z difference between the dopant atom and host [13,19,30]. A second challenge is related to the dynamical scattering of the STEM probe along an atom column [31], which causes probe intensity oscillations along the beam direction (z). It precludes unambiguous interpretation of the contrast in terms of the dopant atom z position for samples that are thicker than half the oscillation period, because the contrast becomes a nonmonotonic function of z [13,21,22,32]. The frequency of the oscillations increases with Z of the host, thus decreasing the allowable thickness [13]. Figure 1(a) shows the simulated probe intensity as a function of foil thickness for $SrTiO_3$ (see the Supplemental Material [33]). The first maximum for the noncorrected probe used here (semiconvergence angle $\alpha = 9.6$ mrad) is located at 3.9 nm, thus defining the upper foil thickness limit. As shown in Fig. 1(a), the period of the oscillations in C_s-corrected STEM ($\alpha = 25$ mrad) is smaller [13], requiring a sample that is thinner than 0.8 nm, which is difficult to obtain.

In this study, we investigate $SrTiO_3$ films, grown by molecular beam epitaxy with Gd concentrations of 0, 0.73, and 3.4 at. %, respectively [33,34]. Figure 1(b) shows a quantitative (i.e., normalized to the incident beam intensity [27]) HAADF-STEM image of the 3.4% Gd sample. Brighter Sr columns are visible (see white square), which may contain Gd. The average thickness of the area in Fig. 1(b) was measured using simultaneous position averaged convergent beam electron diffraction (PACBED) [35], shown in Fig. 1(c). The experimental PACBED pattern (left) matches a simulated pattern of 2.3-nm-thickness (right). However, there are clear thickness variations within Fig. 1(b). The PACBED intensities are dominated by thicker regions, so 2.3 nm is close to the maximum thickness. The experimental PACBED has a slightly higher background, due to diffuse scattering by amorphous surface layers. Both nonuniform thickness and surface layers must be accounted for in the image analysis.

Atom column intensities, I_{col} (col = Sr or Ti-O) were obtained by averaging over a circular region around each column [Fig. 1(d)]. Unlike maximum column intensities, I_{col} are insensitive to parameters that are difficult to determine, such as the effective source size, focus spread, scan noise, sample drift, and Debye-Waller factor [36], and thus allow for direct comparison of experimental I_{col} to simulations [36]. Figures 1(e) and 1(f) show I_{Sr} and $I_{\mathrm{Ti\text{-}O}}$ maps for Fig. 1(b), respectively. Each pixel corresponds to one I_{col} value. The bright Sr column in Fig. 1(b) (white box) exhibits a high intensity in the I_{Sr} map [arrow in Fig. 1(e)]. Its four nearest-neighbor $I_{\mathrm{Ti\text{-}O}}$ [arrow and box in Fig. 1(f)] have similar values relative to the surrounding columns,

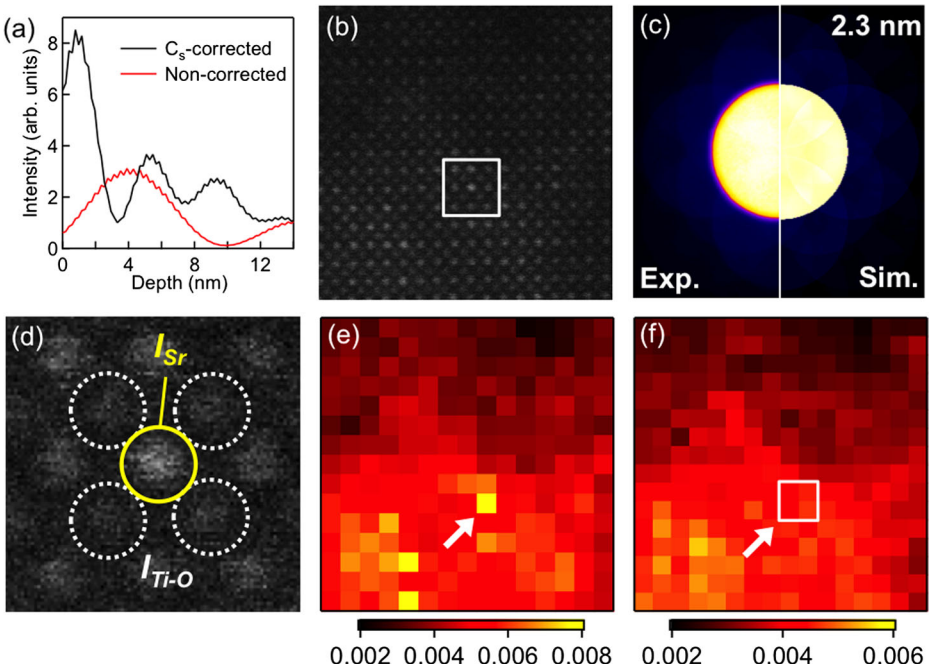

FIG. 1 (color online). (a) Probe channeling characteristics for C_s-corrected and noncorrected probes, respectively. The probe is positioned above a Sr column in $SrTiO_3$, along 100. Weak, superimposed oscillations are due to the dechanneling and rechanneling of the probe as it passes through the individual planes of $SrTiO_3$ (SrO and TiO_2, respectively). (b) HAADF image of 3.4%-Gd-doped $SrTiO_3$. (c) Experimental (left) PACBED pattern from the area shown in (b) and (right) simulated pattern for a 2.3 nm thick sample. (d) Magnified image of the region indicated by the square in (b). The circles indicate the areas over which I_{Sr} and $I_{Ti\text{-}O}$ were averaged. (e) I_{Sr} and (f) $I_{Ti\text{-}O}$ map from the image shown in (b). Scale bars indicate the intensity value normalized to the incident beam intensity.

indicating a uniform local thickness. Thus, the high I_{Sr} must be due to at least one Gd atom in that column.

Toward a quantitative analysis of 3D dopant distributions, we use undoped $SrTiO_3$ to determine the experimental error. Figure 2(a) shows I_{Sr} as a function of $I_{\overline{Ti\text{-}O}}$, where $I_{\overline{Ti\text{-}O}}$ is the averaged intensity of the four Ti-O columns surrounding each Sr column (green open circles). To exclude data affected by thickness variations, only I_{Sr} for which the standard deviation of $I_{\overline{Ti\text{-}O}}$ was less than 4% are included. Multislice simulations (see the Supplemental Material [33]), shown as large filled circles in Fig. 2(a), exhibit lower values than the experimental intensities. This is in contrast to thicker samples (>5 nm), which show excellent agreement [27,37]. The discrepancy for these extremely thin samples (≤ 2.3 nm) is due to non-negligible contributions from amorphous surface (contamination) layers. To account for these, we subtract a background (I_B) from the experimental I_{Sr} and $I_{Ti\text{-}O}$. Results for $I_B = 0.002$ are shown as black triangles in Fig. 2(a). The maximum measured $I_{\overline{Ti\text{-}O}}$ is 0.0032, corresponding to the maximum sample thickness of 6 unit cells (2.3 nm) determined by PACBED, and validates the I_B value used. A two-dimensional (2D) Gaussian error function [inset in Fig. 2(a)] was calculated from the standard deviation of a linear fit to the data [black line in Fig. 2(a)]. The error cutoff was taken to be the full width half maximum of this Gaussian. Likely sources of this error are nonuniform surface layers, sample drift, and electronic noise. We note that the sample has likely no well-defined surface reconstruction or termination, which only develop after appropriate wet-etch and annealing treatments [38].

Figure 2(b) shows I_{Sr} as a function of $I_{\overline{Ti\text{-}O}}$ for Gd-doped $SrTiO_3$, the fit to the undoped $SrTiO_3$ data (solid line), and the error cutoff (dashed line), determined as described above. A total of 24 I_{Sr} and $I_{Ti\text{-}O}$ maps, such as those in Figs. 1(e) and 1(f), from samples containing 0.73% and 3.4% Gd, were used to generate Fig. 2(b). More data points lie above the undoped $SrTiO_3$ line than below it, due to the presence of Gd. The upper dashed line represents the visibility criterion, i.e., the limit of unambiguously identifying the presence of Gd atoms in a column. Columns with intensities above the upper error bound contain at least one Gd atom.

Column intensities were calculated (see the Supplemental Material [33]) for all possible dopant configurations within a Sr column, for one or two Gd atoms, respectively, for the experimental range of foil thicknesses (3–6 unit cells). The probability of having more than 2 dopants in one column is negligible (less than 0.5% for a 2-nm-thick 3.4%-doped sample). The calculated I_{Sr} as a function of $I_{\overline{Ti\text{-}O}}$ are shown in Fig. 2(c) for a 5 unit cell thick region (filled circles). The labels (numbers) indicate the z position of the dopant atom(s), as defined in Fig. 2(d). Two numbers indicate two dopant atoms in a column. I_{Sr}

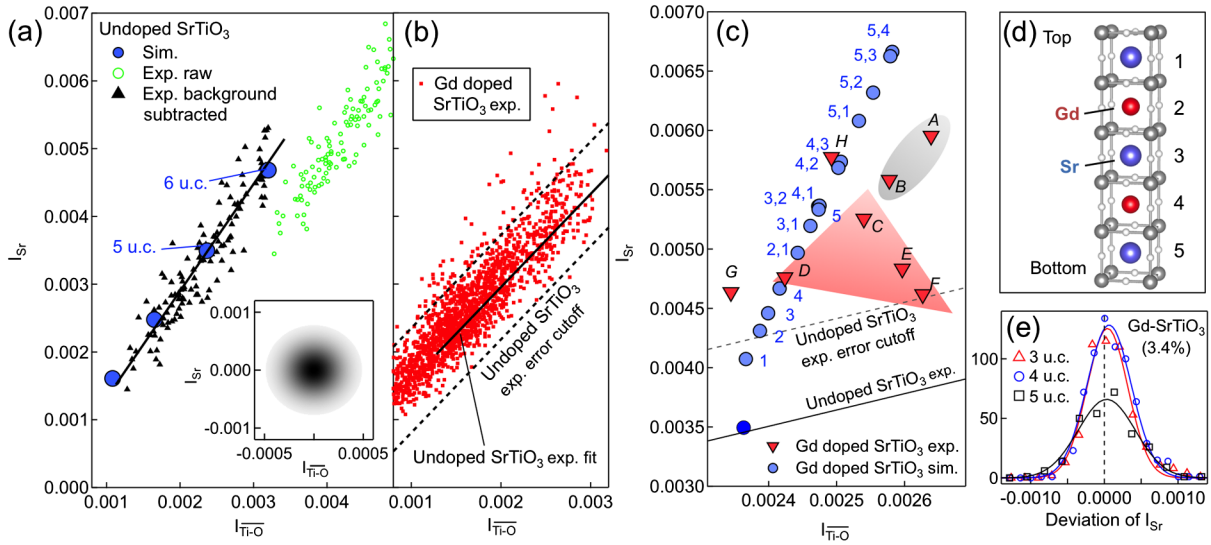

FIG. 2 (color online). (a) Experimental I_{Sr} vs $I_{\overline{Ti\text{-}O}}$ plot for undoped $SrTiO_3$, before (green open circles) and after (black triangles) subtraction of I_B. Multislice simulations are shown as blue filled circles. The inset shows the 2D error function calculated from the experimental data. (b) Experimental I_{Sr} vs $I_{\overline{Ti\text{-}O}}$ plot for Gd-doped $SrTiO_3$ after the background subtraction, and fit for undoped $SrTiO_3$ (solid line). The experimental error as defined by the inset in (a) is also shown (dashed lines). (c) Multislice simulations (blue circles) of column intensities for all possible dopant locations in a 5 unit cell thick region of Gd-doped $SrTiO_3$. The labels (numbers) indicate the dopant position in the column as defined in (d). The filled darker blue circle is the simulation for a 5 unit cell thick undoped $SrTiO_3$. Experimental points, labeled A-G, the undoped $SrTiO_3$ fit from (a) (solid line), and error cutoff (dashed line) are also shown. The large, shaded triangle and the ellipsoid indicate the dopant clusters shown in Figs. 3(a) and 3(b). (e) Histograms of the relative difference between I_{Sr} in Gd-doped and undoped $SrTiO_3$.

monotonically increases as the dopant atom(s) is (are) placed further below the top (entrance) surface. This is expected as the probe intensity increases with depth [Fig. 1(a)]. All possible configurations are above the experimental error cutoff, and are therefore detectable in the measured column intensity, except for the case of a single dopant located in position 1. $I_{\overline{Ti\text{-}O}}$ also increases by a small amount.

The overall dopant concentration can be measured from the I_{Sr}. Using $I_{\overline{Ti\text{-}O}}$, the I_{Sr} of the 3.4% sample are binned according to the nearest $SrTiO_3$ thicknesses (in unit cells). Histograms (see the Supplemental Material [33]) of I_{Sr} relative to I_{Sr} in undoped $SrTiO_3$ for each thickness are shown in Fig. 2(e). All histograms are shifted relative to zero, due to the Gd doping. The relative shift of I_{Sr} in calculations of a known Gd amount with random distribution can be compared to the experimental shift [33]. Extrapolation yields the average dopant concentration, for 3 different thicknesses, of $3.0\% \pm 0.9\%$, which matches well with the Hall measurement of 3.4%. The excellent match validates the analysis method, and shows that essentially all dopant atoms are detected.

Sr columns above the error cutoff line in Fig. 2(b) can be analyzed in terms of the number and z positions of the Gd atoms. As examples, we show in Fig. 2(c) data points from a 5 unit cell thick region, labeled A–H. To match each of these points to a simulated configuration, the experimental error [inset in Fig. 2(a)] needs to be taken into account. For example, for the point labeled H, the error function spans eight nearby simulation points, which are listed in Table I. Please note that the axes of the inset in Fig. 2(a) and 2(c) have different scales. The probability p_i of each of the possible configurations is calculated as $\mathrm{erf}_i(t)/\sum_n \mathrm{erf}_n(t)$, where erf is the error function [inset in Fig. 2(a)], t is how far the simulated point is from the experimental point (in intensity), and n is the total number of simulated configurations spanned by the error function. The probabilities of the possible configurations for data point H are shown in Table I. The probability for H to contain two Gd atoms is ~90%. Calculating the expectation value [39] for

TABLE I. List of all possible dopant depth locations (z_i), defined in Fig. 2(d), for the experimental point H in Fig. 2(c), and their probabilities (p_i) weighted by the 2D error function [shown in 2(a)]. The expectation value is $\sum_i z_i p_i$ [39]. For details see the Supplemental Material [33].

Number of Gd atoms in column	Probability (%)	First atom position	Second atom position	Probability (p_i) for pairs (%)
1	10.31	5	...	...
2	89.69	2	5	6.17
		1	5	16.31
		3	4	25.47
		2	4	24.74
		1	4	11.73
		2	3	10.28
		1	3	5.30
Expectation value		1.9 ± 0.76	4.1 ± 0.61	100.0

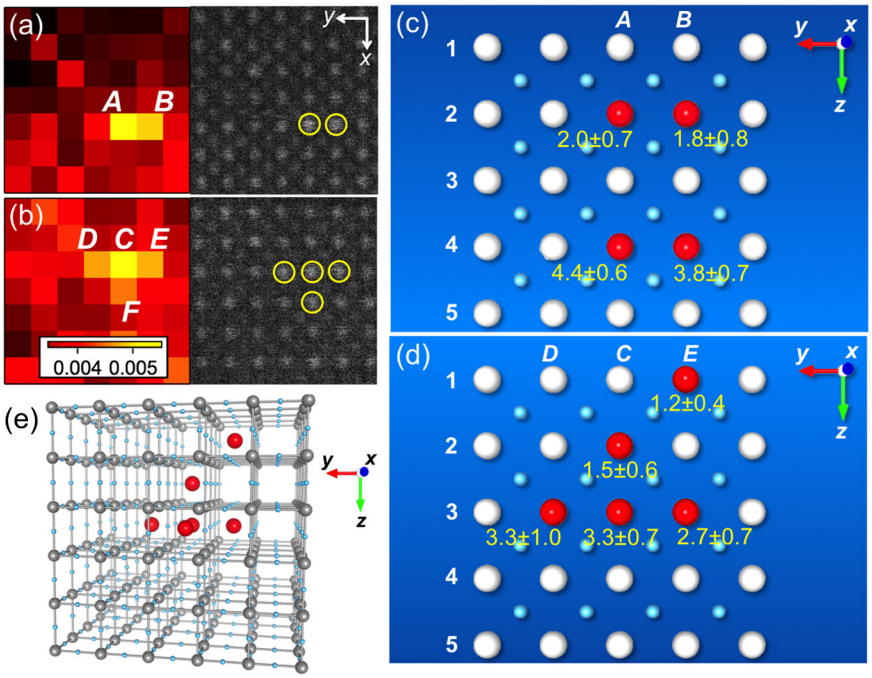

FIG. 3 (color online). (a),(b) I_{Sr} maps (left) and HAADF images (right) of the areas containing A–B columns (a) and C–F columns (b), for which the intensity data were shown in Fig. 2(c). Yellow circles in the images indicate the areas over which the I_{Sr} were averaged. (c),(d) Schematics showing the configurations of dopant atoms in A–B (c) and C–E (d) columns. The most probable dopant position is shown in red and the expectation values and uncertainties are labeled (yellow numbers). (e) 3D illustration of the area in (b) with the most probable Gd dopant configuration in columns C–F. For clarity, Sr atoms are not shown and some Ti and O atoms were also removed.

the first and second dopant atom, respectively, yields the first at position 1.9 ± 0.76, and the second at 4.1 ± 0.61 (see the Supplemental Material [33]). These uncertainties (± 0.24 and ± 0.3 in units of nm) are smaller than one $SrTiO_3$ unit cell (0.3905 nm). Given that Gd must be located on a discrete Sr site, positions 2 and 4 are identified as the most likely positions for these dopant atoms.

The Gd-containing columns labeled A and B, as well as C–F in Fig. 2(c) are adjacent to each other; i.e., they form a small cluster. Images and intensity maps are shown in Figs. 3(a) and 3(b). These are the only clusters in 16 data points analyzed. The depth Gd positions and their probabilities in columns A–G were determined as described above. Figures 3(c) and 3(d) depict the most probable configurations for columns A, B, and C–E, respectively. The labels (numbers) show the expectation values and their uncertainties (see the Supplemental Material [33]). Figure 3(e) shows a 3D representation of the most probable atomic arrangement of the dopant cluster located in columns C–F.

In summary, we have shown that the complete 3D configuration of dopant atoms can be determined from single quantitative STEM images, along with fully quantitative information of expectation values and dopant visibility. Sufficiently thin TEM foils are key for unambiguous interpretation. We note, however, that application of the method to lighter hosts will result in less stringent requirements with regards to the maximum sample thickness, due to reduction in probe oscillations [Fig. 1(a)]. For example, for Si, the sample could be as thick as 10 nm. The expectation values and uncertainties determined here provide evidence for a very high confidence level for a specific 3D dopant atom configuration. The method allows for determination of the overall dopant concentration within small volumes. It applies to a wide range of concentrations and materials. For example, for $SrTiO_3$ with 10% Gd, the probability in a 2 nm sample to have more than 2 Gd atoms in a column is still less than 1.5%. The method can be fully automated, and carried out off-line, allowing for routine analysis of different materials, nanostructures, and devices. Reducing the experimental error should improve the detection of lighter dopants.

The authors thank Pouya Moetakef and Adam Kajdos for providing the samples. J. H. and S. S. acknowledge support by the U.S. Department of Energy (DEFG02-02ER45994). J. H. acknowledges use of the computing facilities of the UCSB Center for Scientific Computing at the California Nanosystems Institute and UCSB MRL (NSF CNS-0960316), which were used to carry out the image simulations. The work made use of central facilities of the UCSB MRL, which is supported by the MRSEC Program of the National Science Foundation under Grant No. DMR-1121053. L. J. A. and A. J. D. acknowledge support from the Australian Research Council's Discovery Project (Project No. DP110102228) and DECRA (Project No. DE130100739).

*To whom correspondence should be addressed.
jhwang@mrl.ucsb.edu
†stemmer@mrl.ucsb.edu

[1] M. Pierre, R. Wacquez, X. Jehl, M. Sanquer, M. Vinet, and O. Cueto, Nat. Nanotechnol. **5**, 133 (2010).
[2] G. P. Lansbergen, R. Rahman, C. J. Wellard, I. Woo, J. Caro, N. Collaert, S. Biesemans, G. Klimeck, L. C. L. Hollenberg, and S. Rogge, Nat. Phys. **4**, 656 (2008).
[3] P. M. Koenraad and M. E. Flatté, Nat. Mater. **10**, 91 (2011).
[4] R. Erni, M. D. Rossell, C. Kisielowski, and U. Dahmen, Phys. Rev. Lett. **102**, 096101 (2009).
[5] P. E. Batson, N. Dellby, and O. L. Krivanek, Nature (London) **418**, 617 (2002).
[6] P. D. Nellist, M. F. Chisholm, N. Dellby, O. L. Krivanek, M. F. Murfitt, Z. S. Szilagyi, A. R. Lupini, A. Borisevich, W. H. Sides Jr., and S. J. Pennycook, Science **305**, 1741 (2004).
[7] D. A. Muller, L. F. Kourkoutis, M. Murfitt, J. H. Song, H. Y. Hwang, J. Silcox, N. Dellby, and O. L. Krivanek, Science **319**, 1073 (2008).
[8] D. Van Dyck, J. R. Jinschek, and F. R. Chen, Nature (London) **486**, 243 (2012).
[9] P. M. Voyles, D. A. Muller, J. L. Grazul, P. H. Citrin, and H. J. L. Gossmann, Nature (London) **416**, 826 (2002).
[10] K. van Benthem, A. R. Lupini, M. P. Oxley, S. D. Findlay, L. J. Allen, and S. J. Pennycook, Ultramicroscopy **106**, 1062 (2006).
[11] S. H. Oh, K. van Benthem, S. I. Molina, A. Y. Borisevich, W. Luo, P. Werner, N. D. Zakharov, D. Kumar, S. T. Pantelides, and S. J. Pennycook, Nano Lett. **8**, 1016 (2008).
[12] H. Okuno, J. L. Rouviere, P. H. Jouneau, P. Bayle-Guillemaud, and B. Daudin, Appl. Phys. Lett. **96**, 251908 (2010).
[13] A. Mittal, and K. A. Mkhoyan, Ultramicroscopy **111**, 1101 (2011).
[14] M. Couillard, G. Radtke, A. P. Knights, and G. A. Botton, Phys. Rev. Lett. **107**, 186104 (2011).
[15] M. Bar-Sadan, J. Barthel, H. Shtrikman, and L. Houben, Nano Lett. **12**, 2352 (2012).
[16] O. L. Krivanek *et al.*, Nature (London) **464**, 571 (2010).
[17] M. Varela *et al.*, Phys. Rev. Lett. **92**, 095502 (2004).
[18] A. A. Gunawan, K. A. Mkhoyan, A. W. Wills, M. G. Thomas, and D. J. Norris, Nano Lett. **11**, 5553 (2011).
[19] M. D. Rossell, Q. M. Ramasse, S. D. Findlay, F. Rechberger, R. Erni, and M. Niederberger, ACS Nano **6**, 7077 (2012).
[20] G. Z. Zhu, S. Lazar, A. P. Knights, and G. A. Botton, Phys. Chem. Chem. Phys. **15**, 11 420 (2013).
[21] P. M. Voyles, D. A. Muller, and E. J. Kirkland, Microsc. Microanal. **10**, 291 (2004).
[22] H. L. Xin, and D. A. Muller, Microsc. Microanal. **16**, 445 (2010).
[23] P. D. Nellist, and P. Wang, in *Annual Review of Materials Research*, Vol 42, edited by D. R. Clarke (Annual Reviews, Palo Alto, 2012), p. 125.
[24] P. Wang, A. J. D'Alfonso, A. Hashimoto, A. J. Morgan, M. Takeguchi, K. Mitsuishi, M. Shimojo, A. I. Kirkland, L. J. Allen, and P. D. Nellist, Ultramicroscopy **134**, 185 (2013).
[25] P. Wang, A. Hashimoto, M. Takeguchi, K. Mitsuishi, M. Shimojo, Y. F. Zhu, M. Okuda, A. I. Kirkland, and P. D. Nellist, Appl. Phys. Lett. **100**, 213117 (2012).
[26] H. L. L. Xin, C. Dwyer, D. A. Muller, H. M. Zheng, and P. Ercius, Microsc. Microanal. **19**, 1036 (2013).
[27] J. M. LeBeau, S. D. Findlay, L. J. Allen, and S. Stemmer, Phys. Rev. Lett. **100**, 206101 (2008).
[28] A. Rosenauer, K. Gries, K. Müller, A. Pretorius, M. Schowalter, A. Avramescu, K. Engl, and S. Lutgen, Ultramicroscopy **109**, 1171 (2009).
[29] J. M. LeBeau, S. D. Findlay, L. J. Allen, and S. Stemmer, Nano Lett. **10**, 4405 (2010).
[30] A. R. Lupini, A. Y. Borisevich, J. C. Idrobo, H. M. Christen, M. Biegalski, and S. J. Pennycook, Microsc. Microanal. **15**, 441 (2009).
[31] M. M. J. Treacy, and J. M. Gibson, Ultramicroscopy **52**, 31 (1993).
[32] R. F. Loane, E. J. Kirkland, and J. Silcox, Acta Crystallogr. Sect. A **44**, 912 (1988).
[33] See Supplemental Material at http://link.aps.org/supplemental/10.1103/PhysRevLett.111.266101 for the methods used for probe intensity and image simulations, sample preparation, imaging parameters, details of the histogram analysis, and the errors given for the expectation values.
[34] J. Son, P. Moetakef, B. Jalan, O. Bierwagen, N. J. Wright, R. Engel-Herbert, and S. Stemmer, Nat. Mater. **9**, 482 (2010).
[35] J. M. LeBeau, S. D. Findlay, L. J. Allen, and S. Stemmer, Ultramicroscopy **110**, 118 (2010).
[36] H. E, K. E. MacArthur, T. J. Pennycook, E. Okunishi, A. J. D'Alfonso, N. R. Lugg, L. J. Allen, and P. D. Nellist, Ultramicroscopy **133**, 109 (2013).
[37] J. M. LeBeau, S. D. Findlay, X. Wang, A. J. Jacobson, L. J. Allen, and S. Stemmer, Phys. Rev. B **79**, 214110 (2009).
[38] A. E. Becerra-Toledo, M. S. J. Marshall, M. R. Castell, and L. D. Marks, J. Chem. Phys. **136**, 214701 (2012).
[39] K. F. Riley, M. P. Hobson, and S. J. Bence, *Mathematical Method for Physics and Engineering* (Cambridge University Press, Cambridge, England, 2006).